Geochemistry, Geophysics, Geosystems

RESEARCH ARTICLE
10.1029/2021GC009745

Key Points:

- This study compares the accuracy of Unmanned Aerial Systems (UAS) scalar and vector magnetometer systems with different suspension designs and compensation methods
- We provide software to process, perform magnetic compensation, and assess the accuracy of UAS scalar and vector magnetometers data
- A fixed frame suspension method combined with magnetic compensation offers flight stability and highly accurate magnetic recordings

Supporting Information:

Supporting Information may be found in the online version of this article.

Correspondence to:

L. Kaub,
lkaub@geophysik.uni-muenchen.de

Citation:

Kaub, L., Keller, G., Bouligand, C., & Glen, J. M. G. (2021). Magnetic surveys with Unmanned Aerial Systems: Software for assessing and comparing the accuracy of different sensor systems, suspension designs and compensation methods. *Geochemistry, Geophysics, Geosystems*, *22*, e2021GC009745. https://doi.org/10.1029/2021GC009745

Received 1 MAR 2021
Accepted 15 JUN 2021

Magnetic Surveys With Unmanned Aerial Systems: Software for Assessing and Comparing the Accuracy of Different Sensor Systems, Suspension Designs and Compensation Methods

Leon Kaub[1], Gordon Keller[2], Claire Bouligand[3], and Jonathan M. G. Glen[4]

[1]Ludwig Maximilians University of Munich, München, Germany, [2]University of California, Santa Cruz, CA, USA, [3]University of Grenoble Alpes, Univ. Savoie Mont Blanc, CNRS, IRD, IFSTTAR, ISTerre, Grenoble, France, [4]U.S. Geological Survey, Moffett Field, CA, USA

Abstract A typical problem for magnetic surveys with small Unmanned Aerial Systems (sUAS) is the heading error caused by undesired magnetic signals that originate from the aircraft. This can be addressed by suspending the magnetometers on sufficiently long tethers. However, tethered payloads require skilled pilots and are difficult to fly safely. Alternatively, the magnetometer can be fixed on the aircraft. In this case, aircraft magnetic signals are removed from the recordings with a process referred to as magnetic compensation, which requires parameters estimated from calibration flights flown in an area with magnetically low-gradients prior to the survey. We present open-source software fully written in Python to process data and compute compensations for two fundamentally different magnetometer systems (scalar and vector). We used the software to compare the precision of two commercially available systems by flying dense grid patterns over a 135 × 150 m area using different suspension configurations. The accuracy of the magnetic recordings is assessed using both standard deviations of the calibration pattern and tie-line cross-over differences from the survey. After compensation, the vector magnetometer provides the lowest heading error. However, the magnetic field intensity recovered with this system is relative and needs to be adjusted with absolute data if absolute intensity values are needed. Overall, the highest accuracy of all suspension configurations tested was obtained by fixing the magnetometer 0.5 m below the sUAS onto a self-built carbon-fiber frame, which also offered greater stability and allowed fully autonomous flights in a wide range of conditions.

Plain Language Summary Mapping the strength of the Earth's magnetic field is widely used for imaging the subsurface in geophysical exploration, detecting unexploded ordnance, and investigating archaeological sites. Small Unmanned Aerial Systems (sUAS), commonly referred to as drones, offer fast, flexible, and affordable aeromagnetic surveys. The main challenge in using sUAS in magnetic surveys is the magnetic signals generated by the sUAS itself, which may swamp out natural geologic signals. In some setups the sensors are attached to the sUAS with long tethers, which are difficult to fly safely. We developed a compact system in which the sensor is attached to the aircraft with a 0.5 m carbon-fiber frame. We correct the magnetic signals caused by the sUAS using a process called magnetic compensation. This requires specific calibration maneuvers performed at the beginning of a survey. We developed software for processing the magnetic data and computing the magnetic compensation. We tested this configuration with two magnetometer systems that are commercially available and compared it to a tethered configuration and a setup where the sensor systems were fixed to the landing gear of the sUAS. The fixed-frame system combined with compensation offers higher flight stability and more accurate magnetic recordings than the other configurations.

1. Introduction

Magnetic surveys have a wide range of applications in the geosciences, including the mitigation of earthquake and volcano hazard assessments (e.g., Finn et al., 2018) and in mineral, petroleum, and geothermal exploration (e.g., Dentith and Mudge, 2014; Nabighian et al., 2005; Hochstein and Soengkono, 1997). Magnetic surveys also are widely used in archeology (e.g., Fassbinder, 2017) and for the detection of unexploded ordnance (e.g., Davis et al., 2010). While ground surveys may provide very high-resolution magnetic data,

they are usually limited in extent and can be heterogeneous in their distribution when access is difficult or dangerous (e.g., Bouligand et al., 2016). On the other hand, typical aeromagnetic surveys acquired using manned aircrafts come with very high financial and logistical costs. Due to recent advances in sensor technology, magnetometers are now small and light enough to be carried by small Unmanned Aerial Systems (sUAS), allowing the acquisition of high resolution and uniformly distributed data at low elevation over large areas. It also enables magnetic surveys in areas difficult to access or that would pose a hazard to pilot and crew on manned flights (e.g., above or near active volcanoes). These systems offer a great deal of flexibility (e.g., since the flight plan can be modified while the survey is being collected), can be flown at a lower cost than commercial airborne surveys, and are now used for a wide range of applications (e.g., Bertrand et al., 2020; De Smet et al., 2020; Gavazzi et al., 2016; Gavazzi et al., 2019; Le Maire et al., 2020; Parvar et al., 2017; Walter et al., 2020).

One of the biggest challenges for sUAS surveys is to minimize the perturbations of the magnetic field caused by movement of the aircraft. One solution is to increase the distance between sensor and aircraft, which for sUAS can be done with long tethers. This, however, limits the flight capabilities for surveys over complex terrain or under high wind conditions that can trigger swinging and twisting motions of the sensor. Our solution is to fix the sensor on a rigid frame attached to the aircraft. While a rigid frame results in larger magnetic perturbations from the aircraft, because the sensor is closer to magnetic sources on the platform, it also permits the characterization and correction of these magnetic signals. By performing calibration maneuvers at the beginning of a survey, we can evaluate the parameters of a model describing the magnetic perturbations of the aircraft. This model is later applied to the survey data allowing for compensation of the aircraft magnetic perturbations. Compensation procedures can be performed using both, scalar magnetometers combined with an Inertial Measurement Unit (IMU) (Leliak, 1961; Tolles and Lawson, 1950), and vector magnetometers (Munschy et al., 2007) but rely on fundamentally different models. For vector magnetometers, the method was designed for the calibration of the sensors (Olsen et al., 2003) but was shown to correct at the same time for perturbations of the aircraft (Munschy et al., 2007).

We created software to compensate for unwanted magnetic signals from the platform. The software includes basic functions, like extracting important data from the raw recordings and interpolating all parameters to the same sampling rate, performing a diurnal correction using data from a stationary base station, computation and application of the compensation parameters, and calculation of discrepancies at flight-line and tie-line crossings necessary for assessing the quality of the magnetic data. Here, we introduce the software and apply it to a dense sUAS magnetic survey to assess the final precision using different sensor types (vector and scalar) and sensor-platform configurations (tethered and fixed frame).

2. Methods

2.1. Compensation Methods

Compensation of the magnetic perturbations of the aircraft is possible in the case of a magnetometer system whose position and attitude remain constant with respect to the aircraft. We use the method of Tolles and Lawson (1950) and Leliak (1961) for the compensation of scalar magnetometer measurements, which has proven to be a reliable way to remove signals from the aircraft (e.g., Hamoudi et al., 2011). Assuming that the intensity of the magnetic field due to the aircraft remains small compared to the intensity of the Earth's magnetic field, Leliak (1961) showed that the intensity of the measured field b_m can be approximated as the sum of the Earth's magnetic field intensity b_0 plus three perturbation terms originating from the aircraft: b_r, caused by remanent magnetizations, b_i by induced magnetizations, and b_e by eddy currents:

$$\overbrace{b_m}^{measured} = \overbrace{b_0}^{Earth's\ field} + \overbrace{b_r + b_i + b_e}^{aircraft\ perturbations}$$

b_r and b_i are associated with ferromagnetic components of the aircraft, while b_e originates from currents that are induced by the movement of electrically conducting parts of an aircraft in the regional magnetic field. For sUAS magnetic surveys, b_e is expected to be small since these aircrafts are small, largely constructed from carbon fiber and plastic, and do not contain large pieces of metal. The expression of the three perturbation terms is derived by projecting the magnetic field vector created by their three sources onto the Earth's

magnetic field vector. The direction of the Earth's magnetic field vector is defined by directional cosines of the field in the aircraft reference frame $\left(\cos X, \cos Y, \cos Z\right)$ along the transverse, longitudinal, and vertical axes.

Since the remanent magnetization is fixed with respect to the aircraft, it creates a magnetic field vector $\boldsymbol{a}$ whose three components are constant in the aircraft frame of reference. The resulting perturbation can therefore be written as (Bickel, 1979):

$$b_r = \boldsymbol{a}^T \boldsymbol{u}$$

where $\boldsymbol{u}$ represents the directional cosines $\left(\cos X, \cos Y, \cos Z\right)^T$ formed by $\boldsymbol{b}_0$ and the axes of the aircraft. These directional cosines are evaluated from the three components of a 3-axis magnetometer, which is usually part of an IMU unit:

$$\cos X = \frac{f_x}{\| \boldsymbol{f} \|_2}, \cos Y = \frac{f_y}{\| \boldsymbol{f} \|_2}, \cos Z = \frac{f_z}{\| \boldsymbol{f} \|_2}$$

with $\boldsymbol{f} = \left(f_x, f_y, f_z\right)^T$.

The magnetic field vector produced by induced magnetization at the location of the magnetometer is expressed as the product of a 3×3 matrix (denoted as $\boldsymbol{B}$ with coefficients B_{ij}) and the Earth's magnetic field vector $b_0\boldsymbol{u}$. According to Bickel (1979), the resulting magnetic perturbation can therefore be written as:

$$b_i = b_0 \boldsymbol{u}^T \boldsymbol{B} \boldsymbol{u}$$

This expression corresponds to the sum of 9 terms. Since $B_{ij} = B_{ji}$, the magnetic perturbations due to induced magnetizations are defined by six coefficients (Leliak, 1961). Furthermore, since $\cos^2 X + \cos^2 Y + \cos^2 Z = 1$, one of the terms $B_{ii} b_0 u_i^2$ can be eliminated leaving a constant term $-B_{ii} b_0$, which can be filtered out by applying a high-pass filter to the measurements of the magnetic field intensity from the maneuvers. This results in one of the B_{ii} being zero, leaving five remaining independent coefficients.

Finally, the eddy current term can be written as:

$$b_e = b_0 \boldsymbol{u}^T \boldsymbol{C} \frac{\mathrm{d}\mathbf{u}}{\mathrm{dt}}$$

with $\boldsymbol{C}$ being a 3×3 matrix consisting of coefficients C_{ij}. Taking the time derivative of $cos^2 X + cos^2 Y + cos^2 Z = 1$ leads to $\cos X \, \mathrm{d} \cos \mathrm{X} / \mathrm{dt} + \cos Y \, \mathrm{d} \cos \mathrm{Y} / \mathrm{dt} + \cos Z \, \mathrm{d} \cos \mathrm{Z} / \mathrm{dt}$ showing that one of the terms C_{ii} in the above equation can be eliminated, which leaves eight independent coefficients (Bickel, 1979). The temporal derivatives of the directional cosine involved in the expression of the eddy current perturbations are computed after applying a low-pass filter to the fluxgate data that reduces noise.

The resulting 16 parameters of the model are inverted from calibration maneuvers performed in a low gradient area. After filtering out the long-wavelength components from b_m to remove b_0 and its spatial variations recorded during these maneuvers, the remaining signal can be fully assigned to interference from the aircraft. A ridge regression inversion is performed to find the model parameters best fitting the interference signals. The model can then be applied to the actual survey data to compensate for the aircraft's signal. The success of the model calibration relies on the relative strength of the interfering signals with respect to the amplitude of spatial variations of the Earth's magnetic field at the location of the calibration maneuvers and on finding the optimum filter settings to separate interference signals from geologic signals.

For the compensation of the 3-axis vector magnetometer measurements, we use the non-linear inverse method proposed by Munschy et al. (2007). Here, we are interested only in recovering the intensity and not the three components of the magnetic field. The purpose of this procedure is not only to remove the magnetic perturbations of the aircraft but also to correct for miscalibration of the fluxgate sensors which include three types of calibration parameters: the offset between the output value of the three sensors and the actual field value, the sensitivity of the sensors which is the ratio between relative changes in output values and

in the actual field values, and non-orthogonality of the three sensors. These three later sources of error can be corrected with a model defined by 9 parameters (Olsen et al., 2003), where the measured magnetic field vector $\boldsymbol{b_m}$ is related to the Earth's magnetic field vector $\boldsymbol{b}_0$ as follows:

$$\boldsymbol{b_m} = \boldsymbol{SPb}_0 + \boldsymbol{o}$$

$\boldsymbol{P}$ is a matrix transforming the three components of the Earth's magnetic field from an orthogonal to non-orthogonal frame, $\boldsymbol{S}$ the diagonal matrix of sensitivities, and $\boldsymbol{o}$ the offset vector:

$$\boldsymbol{S} = \begin{bmatrix} S_1 & 0 & 0 \\ 0 & S_2 & 0 \\ 0 & 0 & S_3 \end{bmatrix}, \boldsymbol{P} = \begin{bmatrix} 1 & 0 & 0 \\ -\sin P_1 & \cos P_1 & 0 \\ \sin P_2 & \sin P_3 & \sqrt{1-\sin^2 P_2 - \sin^2 P_3} \end{bmatrix}, \text{and } \boldsymbol{o} = \begin{bmatrix} o_1 \\ o_2 \\ o_3 \end{bmatrix}$$

Munschy et al. (2007) showed that the remanent and induced magnetizations of an aircraft are accounted for with this model, while it does not incorporate eddy currents. Nevertheless, these are not expected to be very important for sUAS as explained earlier. Knowing the 9 model parameters, $\boldsymbol{b}_0$ and its intensity can be recovered as follows:

$$\boldsymbol{b}_0 = \boldsymbol{P}^{-1}\boldsymbol{S}^{-1}\left(\boldsymbol{b_m} - \boldsymbol{o}\right)$$

$$b_0 = \sqrt{\left(\boldsymbol{b}_0\right)^T \boldsymbol{b}_0} = \sqrt{\left(\boldsymbol{P}^{-1}\boldsymbol{S}^{-1}\left(\boldsymbol{b_m} - \boldsymbol{o}\right)\right)^T \boldsymbol{P}^{-1}\boldsymbol{S}^{-1}\left(\boldsymbol{b_m} - \boldsymbol{o}\right)}$$

Model parameters are estimated from measurements performed during calibration maneuvers by minimizing, with a least-square approach, the difference between the norm of the magnetic vector measured by the 3-axis vector magnetometer after correction and the known intensity of the magnetic field at that location. This method was originally developed by Olsen et al. (2003) for the calibration of a vector magnetometer using the intensity of the magnetic field measured by a scalar magnetometer. Since we do not measure the intensity with an additional magnetometer on board the aircraft when working with sUAS, we use here a constant value of the intensity of the magnetic field as suggested by Munschy et al. (2007). This may cause the final intensity map to include an offset as we typically do not recover the exact magnetic field intensity at the location of the calibration maneuvers. Such offset is however not critical for magnetic anomaly studies or can be corrected for as discussed later.

For both methods, the quality of the compensated data is assessed by computing the standard deviation of the compensated intensity data during the calibration pattern. We also compute an improvement ratio (IR) from the standard deviation σ of the raw (uncompensated) and compensated measurements during the maneuvers: $\text{IR} = \sigma_{\text{raw}} / \sigma_{\text{compensated}}$.

2.2. Hardware

We are working with total-field scalar magnetometer (SM, Figure 1a) and vector magnetometer (VM, Figure 1e) systems that are both designed to be carried by sUAS. Each system contains two magnetometers, a data logger, a GNSS unit and a Lithium-ion battery power source. The SM (MagArrow, Geometrics, Inc.) contains two miniature, high-resolution Cs-vapor magnetometers (MFAM, Geometrics, Inc.) that are placed side by side in the rear part of the system and oriented with an angle of 90° between their optical axes. A weighted average of the measurements from the two MFAM sensors prevents dead zones, which are spatial orientations where a magnetometer loses its sensitivity and a typical limitation of optically pumped magnetometers (Acuña, 2002). This system also contains an IMU unit consisting of accelerometers, gyroscopes, and a compass (three-axis anisotropic magnetoresistance magnetometer) allowing to recover the attitude of the system. The VM (MagDrone R3, SenSys - Sensorik & Systemtechnologie GmbH), on the other hand, has two three-axis fluxgate magnetometers, which are located one meter apart at each end of a carbon fiber tube. The system automatically applies a calibration and an offset correction (that accounts for the influence of temperature) to both sensors. These corrections are based on parameters that are stored

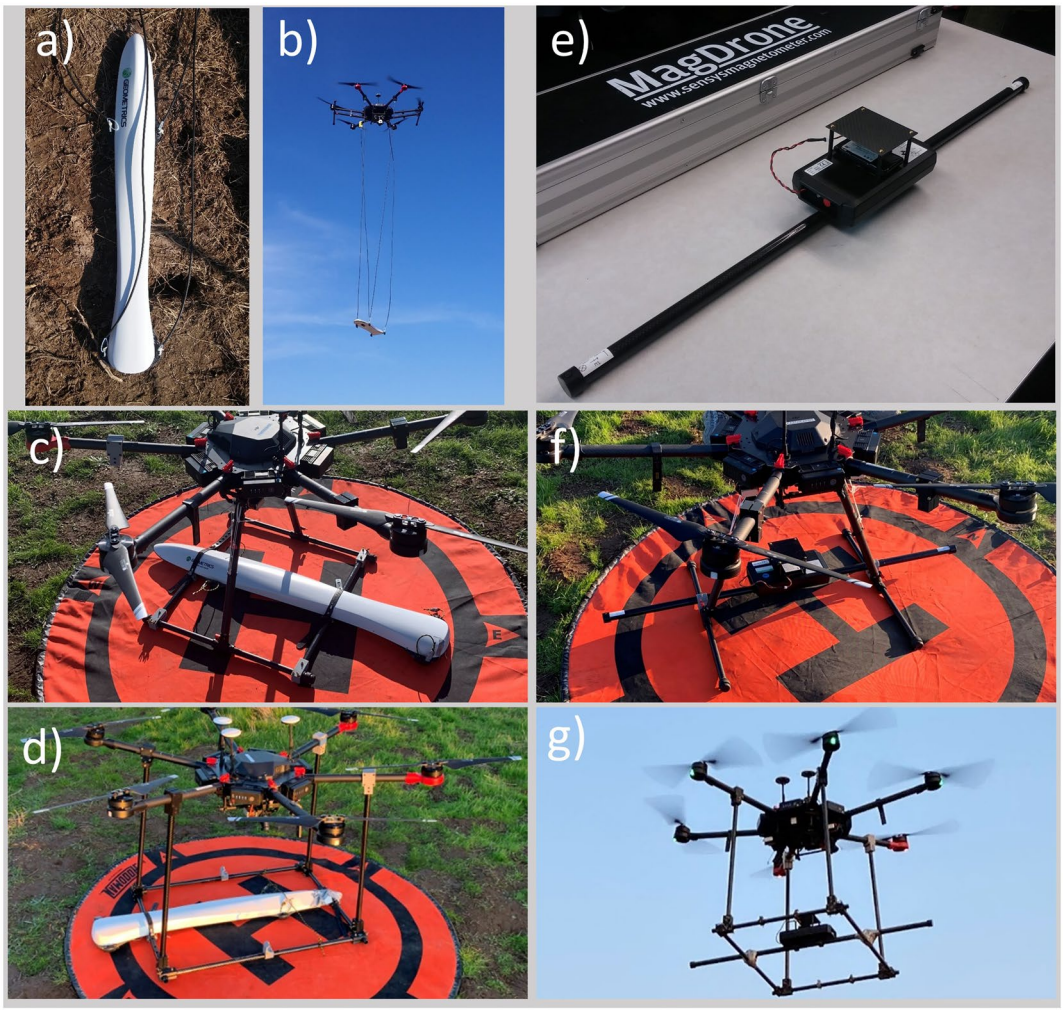

Figure 1. Photos of the two magnetometer systems and their suspensions: MagArrow system (a) flown with a DJI Matrice 600 Pro on 2.8 m tethers as suggested by the manufacturer (b), attached to the landing gear using two additional crossbars (c), and on our fixed frame (d). MagDrone system (e) attached to the landing gear of the Matrice 600 Pro as suggested by the manufacturer (f) and flown on our frame (g).

internally and provided by the manufacturer, which recommends updating them every 4 years. Note that such manufacturer recalibration of the sensors may not be necessary as the compensation method for the VM presented above can also be used to correct for miscalibration of the sensors. Although we focused in this study on surveying the intensity of the magnetic field, the VM could potentially be used for full-vector and/or gradiometry studies as well. However, recovering the vector of the magnetic field would require additional high-precision gyroscopes, which are not part of the VM. Some specifications of both magnetometer systems are given in Table 1.

The platform we used was a hexacopter (Matrice 600 Pro, DJI Technology Co., Ltd.) with a size of 1.67 × 1.52 × 0.76 m (propellers, frame arms, GPS mount, and landing gear unfolded) and a weight of ~10 kg. It has a payload capacity of 5.5 kg, greatly exceeding the weight of the sensor systems (see Table 1). According to the manufacturer, this platform has a theoretical flight time of ~35 min for a 1 kg payload. In practice, however, we have found during our experiments that flight times are typically shorter (in the range of 20–25 min), due to weather conditions, flight maneuvers, and battery cycles.

The two magnetometer systems are designed to be attached to the aircraft in different configurations. The manufacturer of the VM indicates that the unit should be fixed to the aircraft. Therefore, we designed and 3D-printed joints to attach the magnetometer system to the landing gear of the sUAS (Figure 1f). As part

Table 1
Selected Specifications of the Two Magnetometer Systems (Geometrics Inc., 2019; SENSYS, 2018)

System	Scalar magnetometer	Vector magnetometer
Sensor	Optically pumped Cs-vapor	3-axis fluxgate
Length	1.05 m	1.08 m
Weight	1 kg	0.9 kg
Direction of long axis	Parallel to flight direction	Transverse to flight direction
Sampling rate	1,000 Hz	200 Hz
Sensitivity	5 pT/√Hz rms typical	<15 pT/√Hz @ 0.1–10 Hz
Battery	~2h	~3 h

of our tests, we also developed a way to attach the SM to the landing gear by using adjustable rubber straps to fix the SM to carbon fiber crossbars that connect the two landing gear skids (see Figure 1c). For both magnetometer systems, the landing gear configuration additionally required disabling motors on the sUAS that normally pull up the landing gear after take-offs, as well as replacing potentially magnetized springs that hold the landing gear with nonmagnetic cable ties. The SM is designed to be hung from the platform with four tethers that are long enough so that magnetic effects of the aircraft can be neglected (2.8 m was recommended by the manufacturer, see Figure 1b). To make the system more compact and easier to fly and to provide a solid suspension for the magnetometer systems, we designed a rigid frame out of carbon fiber tubes that can hold the sensors 0.5 m below the main body of the platform (Figures 1d and 1g). Since the landing gear was shorter than 0.5 m, the frame also acts as a new landing gear allowing removal of the original. Both magnetometer systems can be attached to the same frame. The carbon fiber tubes are connected to the platform as well as to ech other with joints that were 3D-printed using ABS plastic.

2.3. Software

Here we present MagComPy–software that was developed for working with data from the above-described magnetometer systems (Kaub, 2021). It was designed to be adaptable also to other sensor systems that are used in aerial magnetometry. MagComPy is fully written in Python and therefore platform independent and easy to install. A user-friendly interface allows access to these modules, but they also can be used in user-developed scripts. The software can be used for many tasks that are usually done with airborne magnetic recordings, including the merging of drone and base-station magnetometer recordings, compensating magnetic perturbations that originate from the aircraft, and computing cross-over differences. All results presented in this paper were computed using MagComPy. Any further analysis and interpretation of the data (e.g., reduction to the pole, modeling, mapping) will have to rely on more advanced software. There is an open-source solution for these tasks available called Generic Mapping Tools (GMT), that can be accessed through several programming languages including Python (Wessel et al., 2019).

2.3.1. File Preparation

The two magnetometer systems used for this study record data in sensor-specific binary formats. Therefore, the raw recordings are first converted to a comma-separated values (CSV) format with software tools provided by the manufacturers. These converted files contain signals from different sensors (magnetometer, GNSS, IMU) that are merged but sampled at different frequencies. The “file preparation” tool resamples the different signals at a common frequency and optionally merges these data with data from a base station magnetometer for diurnal corrections. If available, the data can also be merged with GNSS data from the sUAS's flightlog, which are generally of higher accuracy than the magnetometer GNSS data. The tool is designed to be easily adapted to changes in the input file formats that might come with firmware updates of the magnetometer systems or sUAS. The software is designed to facilitate the processing of data from other magnetometers, sUAS, and attachment configurations. Even though the magnetometer systems work with fundamentally different sensors, the general tasks are similar for both the vector and the scalar systems. In a first step, the tool reads the recording coordinates and plots the flight path. During this step, the user can trim the data to remove recordings that are not part of the intended survey (e.g., acquired during takeoffs

and landings or while the sUAS is on the ground) or to separate multiple surveys gathered in one data file. Trimming the data has proven to be a valuable feature as it significantly decreases the size of the output file and significantly expedites the remaining processing. In a second step, the tool extracts the important data from the recording and resamples all signals to the same sampling rate–typically the sampling rate of the magnetometer. Finally, the tool converts the longitude and latitude coordinates into projected coordinates for a given coordinate system chosen by the user. Base station data, if available, are interpolated to the common sampling rate and used for diurnal correction of the magnetic field data. The option to use GNSS data from the sUAS is currently limited to platforms from DJI which let you retrieve flightlog files with data from the GNSS/IMU units that we convert to a CSV format with a third-party software tool (https://datfile.net/DatCon/intro.html). For higher precision positioning data, differential GNSS could be used by mounting an external GNSS sensor on the aircraft and installing a GNSS base-station. Merging such differential GNSS data with data from the magnetometer systems would require some changes in MagComPy regarding the data format of the GNSS files but is in principle possible.

2.3.2. Compensation

Software tools were also designed for the compensation of both scalar and vector magnetic data. Both tools can be used to compute model coefficients from calibration flights that can later be applied to survey data. Program inputs include: ascii formatted data files, scalar magnetic field intensity at the location of the calibration flight (used in the vector compensation only), and filter corner frequencies (used in the scalar compensation only). Corner frequencies are required for both the high-pass filter that is used to remove the geomagnetic signals and the low-pass filter that is applied before the computation of the directional cosine derivatives. In the software, we use a fourth-order Butterworth filter and corner frequencies normalized from 0 to 1, where 1 is the Nyquist frequency (0.5 * sampling rate). To find the optimal corner frequencies, parameter sweeps can be used to compute the IRs for a list of specified frequencies. This enables selecting frequencies based on maximum improvements of the signals. Both scalar and vector compensation tools create plots for validating the proper compensation of the data and save the resulting data to ascii files. Such ascii files can easily be imported in other software (e.g., GMT) for further processing.

2.3.3. Cross-Over Differences

A good way to assess the quality of the compensation is to calculate the differences of the magnetic field values at intersections of flight lines (e.g., Telford et al., 1990), since the magnetic field intensity measurements should be independent of the flight direction. Differences at these intersections can be caused by errors of the magnetic sensors (heading errors or drifts), incomplete compensation of the magnetic fields arising from the aircraft, and errors in the positioning (horizontal and vertical) of either the magnetometer system or the sUAS. As part of our software, we created a tool that can be used to calculate differences at cross-over points, called cross-over differences. The input data can be any file (CSV format) containing projected coordinates and the corresponding signals to assess. The tool first simplifies the flight path into a succession of straight sections using the Ramer-Douglas-Peucker (RDP) algorithm (Douglas and Peucker, 1973; Ramer, 1972) and then finds turning points based on the angle between adjacent sections. Two parameters can be set to control the computation of turning points: the distance dimension epsilon of the RDP algorithm, which corresponds to a tolerance distance between the real flight path and the simplified path, and the minimum angle that defines a turning point. The turning points are then used to divide the survey into segments that can be classified, based on their azimuth, as either a flight line or a tie line, or are discarded if they are shorter than a specified minimum length or their azimuths are not in the specified range. The tool then searches and calculates the location of cross-over points at the intersection of flight lines and tie lines. Finally, the magnetic field values from the flight lines and tie lines are interpolated at the cross-over points and used to compute the cross-over differences. The magnetic field data can be low-pass filtered before calculating the cross-over differences using a fourth-order Butterworth filter. The cross-over differences can be computed for any signal available in the CSV file (e.g., uncompensated and compensated magnetic field intensity, altitude, etc.) and be saved along with the location of cross-over points to a text file for further analysis. This tool cannot be used to apply leveling corrections, a procedure commonly done in magnetic surveys to further correct for potential drift or residual heading errors in the data. For these processing steps, further software needs to be used as for instance GMT, which includes packages for analyzing cross-over differences as well as computing and applying leveling corrections (Wessel, 2010; Wessel et al., 2019).

2.4. Test Survey

To test our magnetometer systems and the different suspensions described above, we designed a high-resolution grid survey with 11 flight lines and 10 tie lines covering an area of more than 135 × 150 m located at the campus of the University of California, Santa Cruz (USA). We flew this survey with the SM on three configurations-tethers, on frame, and on landing gear- and with the VM on the frame and on the landing gear. The survey was acquired at a constant altitude of 30 m above the takeoff point to assure that the cross-over differences were not affected by a difference in flight altitude. However, due to a mistake while using the flight control software, the tethered configuration was flown about 10 m below the other surveys. We further tested the performance of the compensation methods by repeating some of the surveys in the opposite direction. Additionally, we did calibration flights with each of the fixed configurations at a location with low magnetic gradient, which was known from a previous magnetic survey. The pattern was flown at 120 m altitude above ground, which is the maximum flight altitude allowed under regulations of the Federal Aviation Administration, to further minimize any magnetic gradient. As a calibration flight we used an asterisk pattern consisting of eight 40-m long lines, four of which were aligned with the flight direction of the main survey lines and tie lines (see Figures S1 and S2 (e.g., of the SM and the VM, respectively). The 40-m length of the pattern lines were chosen so that the UAS was able to reach the survey speed (7 m/s) and thereby the survey pitch angles along these lines. It is worth mentioning that others (e.g., Gavazzi et al., 2019) are using smaller calibration patterns. More tests are needed to verify whether reaching the survey speed and pitch angle during the calibration procedure is necessary. The surveys were acquired using curved turns, whereas during these calibration pattern flights the sUAS stopped and rotated towards the next waypoint at the end of each line. To account for the diurnal variations of the geomagnetic field, a base station (G856 proton magnetometer, Geometrics, Inc.) constantly recorded the field intensity at a fixed location close to the test site. All parameters that were used to compute the magnetic compensations for the SM and the VM can be found in Tables S1 and S2, respectively.

The readings from fluxgate sensors are known to drift with time (e.g., Ripka, 1992), and the magnetic and electrical properties of the platform may also slightly change during field work, transportation, or storage. It is therefore reasonable to ask whether these changes are significant over the duration of a given survey that typically span several days but may extend over several months or years in the case of long-term studies. The practical reason to address this is to determine the necessity to repeat the calibration flight to update the compensation parameters in order to merge the different parts of a survey. To investigate this, we collected vector magnetic data over a calibration pattern that was repeated at different dates during a week-long period. The calibration pattern was flown at an elevation of 120 m in an area of low magnetic gradient at Surprise Valley in Northern California using a clover-leaf pattern rather than the asterisk pattern discussed previously (see Figure S3).

3. Results

Both compensation methods for the SM and the VM depend on data collected during a calibration flight at a location with low magnetic gradient. Ideally, the compensated signals should have all effects from the aircraft removed, resulting in a constant signal during the calibration flight. Figure 2 shows that the recordings from both the scalar magnetometer system and the vector magnetometer system (which includes two sensors, noted 1 and 2) in the frame and landing gear configurations display large fluctuations. These fluctuations are largely removed after compensation, leaving a relatively constant high frequency noise likely due to the sUAS motors. Some locally larger fluctuations that were not fully removed by the compensation are associated with abrupt turns in the asterisk-shaped calibration pattern, which can be observed in Figures S1b and S2b.

Depending on the magnetometer system and the configuration (frame vs. landing gear), we obtain improvement ratios from the calibration flights that vary from about 4 to 10 and standard deviations of the compensated signal, σ_{comp}, that vary from 4.4 to 7.5 nT (Table 2). For the VM system, improvement ratios from sensor 1 are systematically larger than the ones from sensor 2 but this appears to be due to the larger standard deviation of the uncompensated signal, σ_{raw}, of sensor 1 whose factory calibration is likely inferior. The landing gear configuration leads systematically to larger standard deviation of the compensated signal

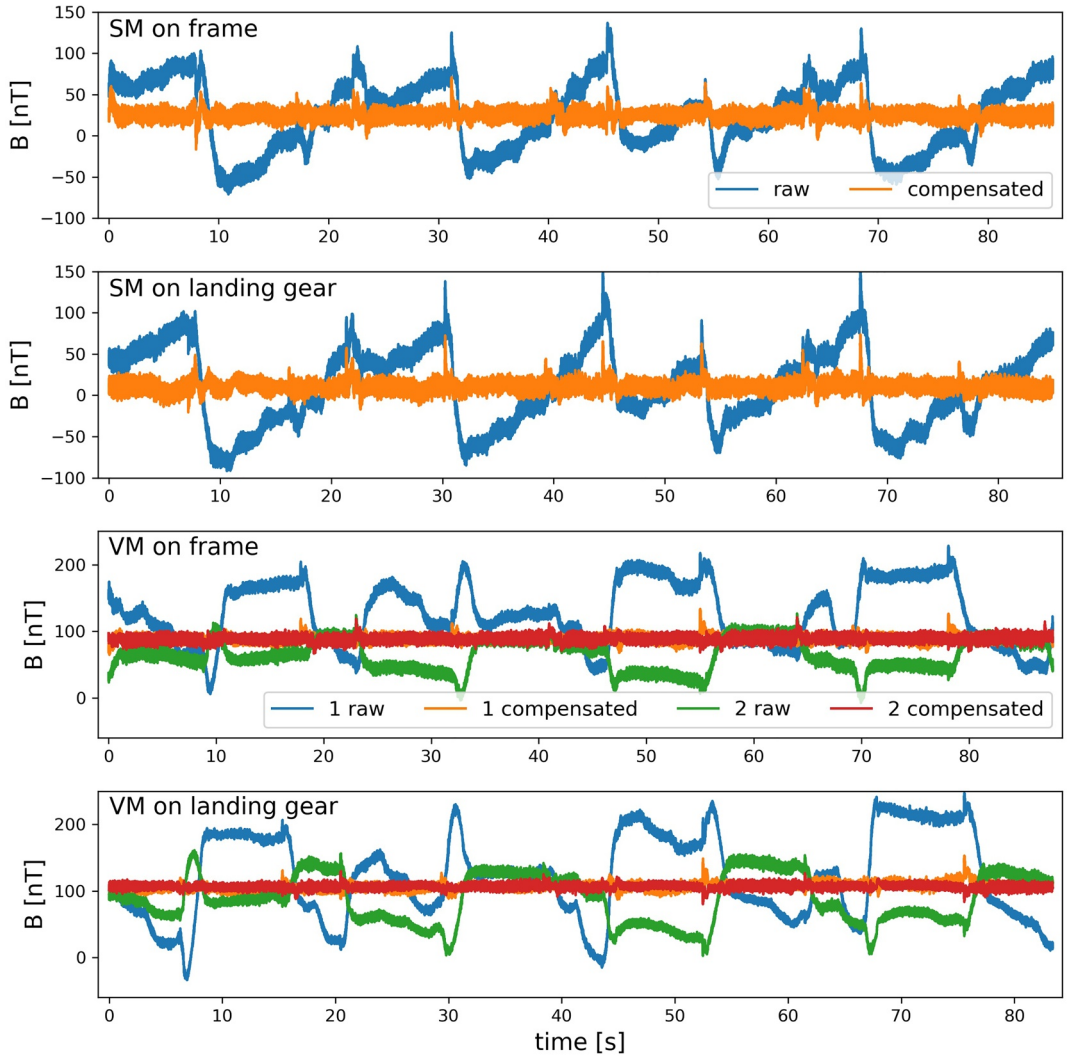

Figure 2. Effect of compensation on the magnetic field intensity during asterisk-shaped calibration flights: magnetic field signals are plotted for the scalar magnetometer system (SM) and the vector magnetometer system (VM) and for each suspension configuration (frame and landing gear), before and after compensation. VM is recording with two sensors 1 and 2 that are compensated independently. Note that the scale of the y-axis is the same for the two configurations of the respective sensor systems.

likely since the sensors are closer to the sUAS compared to the frame configuration. We additionally computed standard deviations after applying a low-pass filter, $\sigma_{\text{comp,lp}}$, where we used filter settings based on the analysis of cross-over differences shown below.

We also compare the standard deviation of the uncompensated and compensated signal (σ_{raw} and σ_{comp}) for the survey data in a combined plot (Figure S4). The standard deviations were computed from the survey line and tie line data after discarding turns and short segments. These standard deviations are larger than the ones obtained from the calibration patterns as they reflect both magnetic perturbation from the aircraft and geological signals. Nevertheless, Figure S4 shows that the systems that were flown in two directions (normal and reversed) lead to very similar standard deviations after compensation. The differences between σ_{comp} of the normal and the reversed flights ranged from 0.2 nT (SM on landing gear) to 0.8 nT (VM on frame).

As explained above, the improvement that is accomplished by magnetic compensation of the recordings can be quantified by computing cross-over differences. An example of this for VM sensor 2 is shown in Figure 3. While the uncompensated signal results in large heading errors and cross-over differences (Figures 3a

Table 2
Standard Deviations of the Uncompensated Signals (σ_{raw}), the Compensated Signals (σ_{comp}), and the Compensated Signals After a Low-Pass Filter was Applied ($\sigma_{comp.lp}$), Together With the Improvement Ratios (IR) From Calibration Flights With Each Configuration

Magnetometer	Suspension	Sensor	σ_{raw} [nT]	σ_{comp} [nT]	IR	$\sigma_{comp.lp}$ [nT]
Scalar	Frame		41.8	6.8	6.1	1.7
Scalar	Landing gear		46.4	7.5	6.1	3.5
Vector	Frame	1	46.7	5.6	8.4	2.6
Vector	Frame	2	23.6	5.5	4.3	2.2
Vector	Landing gear	1	63.9	6.3	10.1	5.3
Vector	Landing gear	2	37.1	4.4	8.5	1.9

Note. The IR was computed using σ_{comp} before filtering.
Abbreviation: IR, Improvement ratio.

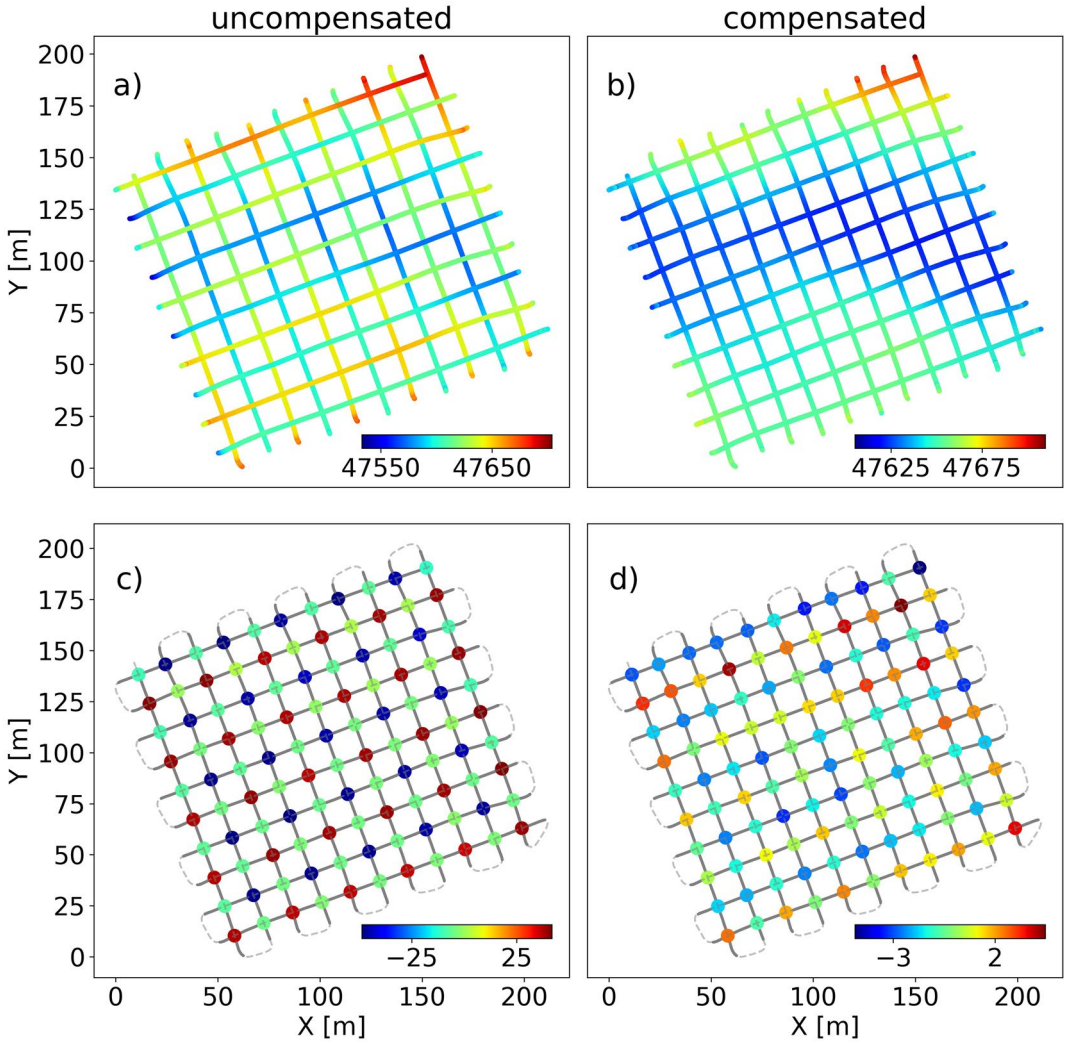

Figure 3. Example of magnetic field intensity data (in nT) and cross-over differences (in nT) from sensor 2 of the vector magnetometer attached to the frame setup before and after compensation: uncompensated (a) and compensated recordings (b), cross-over differences for uncompensated (c) and compensated recordings (d). Used lines are plotted as gray solid lines and dismissed segments shown with dashed lines for figures (c) and (d).

Table 3
RMS of Cross-Over Differences for all Flown Surveys Using the Compensated Signals

Magnetometer	Suspension	Flight direction	Sensor	RMS [nT]	$\mathbf{RMS_{lev}}$ [nT]
Scalar	Tethers	Normal		5.2	2.0
Scalar	Frame	Normal		3.3	1.9
Scalar	Landing gear	Normal		5.1	2.1
Scalar	Landing gear	Reversed		4.8	3.3
Vector	Frame	Normal	1	2.2	0.6
Vector	Frame	Normal	2	2.1	1.6
Vector	Frame	Normal	Average	1.6	
Vector	Frame	Reversed	1	2.2	1.9
Vector	Frame	Reversed	2	2.3	1.9
Vector	Frame	Reversed	Average	1.8	
Vector	Landing gear	Normal	1	6.6	4.1
Vector	Landing gear	Normal	2	6.5	2.5
Vector	Landing gear	Normal	Average	5.5	
Vector	Landing gear	Reversed	1	13.0	3.3
Vector	Landing gear	Reversed	2	8.0	8.0
Vector	Landing gear	Reversed	Average	7.9	

Note. Signals were low-pass filtered with filter corner frequencies that resulted in minimum RMS values (see Table S3). For the VM, both sensors as well as a dual sensor average were analyzed. RMS values were computed using MagComPy (Kaub, 2021), while leveling corrections and RMS values after leveling ($\mathbf{RMS_{lev}}$) were computed using commercial software (Oasis montaj, Seequent).
Abbreviation: RMS, Root mean square.

and 3c), only small heading errors are observed in the compensated signal (Figures 3b and 3d). This improvement is observed in all tested configurations.

The cross-over differences can be analyzed by computing their root mean square (RMS) values. We computed RMS values for the surveys flown with each configuration that consisted of 11 flight lines and 10 tie lines resulting in 110 cross-over locations (Table 3). The magnetic field signals have been low-pass filtered before cross-over differences were computed to avoid effects from high-frequency components. The filters were applied using corner frequencies that resulted in minimum RMS values of the cross-over differences (see Table S3). For the VM, we computed cross-over differences for each of the two sensors as well as for the dual sensor average.

The distributions of the cross-over differences are also plotted as box-and-whisker plots in Figure 4. The results show that (a) the frame configuration results in the lowest heading errors for both sensor systems (cross-over differences have a range of 6.4 nT for the SM and 3.1–4.6 nT for the VM), (b) the largest heading errors are observed for the landing gear configuration, which are comparable for both sensor systems and similar to those of the SM tethers configuration, (c) the flight direction has little influence on the SM using the landing gear and the VM using the frame suspension, but we observed significantly larger cross-over differences for the reverse flights of the VM with the landing gear configuration, and (d) there is no consistent difference between the two sensors of the VM and the lowest heading errors are achieved with the dual sensor average.

The cross-over differences obtained after compensation can be further decreased by applying leveling corrections to the surveys. Leveling is a standard processing step used for the analysis of aeromagnetic data to remove residual heading error or drift in the data. Since MagComPy does not include a leveling module, we used commercial software (Oasis montaj, Seequent) to compute leveling corrections by applying a 4-th order trend to all tie-lines and then adjusting the flight-lines to match the leveled tie-lines. This correction systematically led to smaller RMS values (Table 3). We also see that after applying this correction our above conclusions (1–4) remain unchanged.

Using positioning data from the sUAS did not improve cross-over differences compared to using positioning data from the magnetometer systems. The figures and the cross-over difference analysis shown here are therefore based on the magnetometer systems GNSS data. The sUAS data was however used to analyze the altitude measured by the sUAS, which led to RMS values of altitude cross-over differences below 0.1 m.

We further used calibration flights collected over a week-long period in Surprise Valley, CA, with the VM on the frame setup to estimate how the quality of the compensation of the VM degrades over time. For each acquisition of the calibration pattern, we estimated a best-fit set of compensation parameters (noted best). Diurnal variation of the Earth's magnetic field was accounted for when providing an absolute value of the field intensity in the application of the vector calibration. To do this, we selected an arbitrary value for the first acquisition of the calibration pattern and then adjusted this value for the next acquisitions based on the recordings from a fixed base-station. Each calibration pattern was also compensated using the set of parameters deduced from the first acquisition of the calibration pattern chosen as a reference (noted first). Then, we compared the quality of the compensated data obtained using both the first and best sets of parameters. Figure 5 and Table 4 show results from sensor 1 (similar to results from sensor 2) with recordings from four different days each spaced two days apart. We see that standard deviations are slightly increased when using the first set of parameters (σ_{first} larger than σ_{best} in Table 4) but this increase does not appear significant when compared to variations of the standard deviation for the different recordings (see variations of σ_{best}

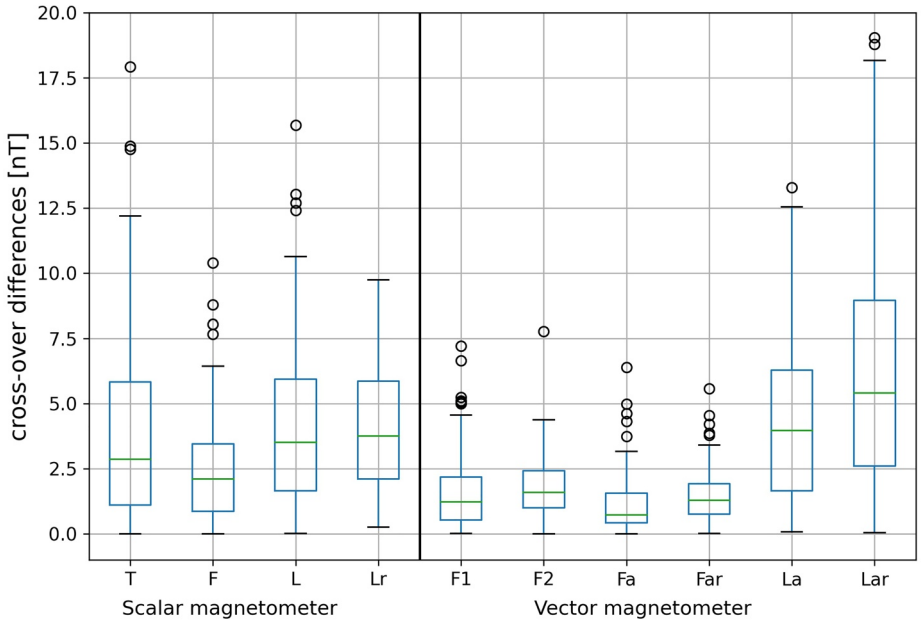

Figure 4. Cross-over differences for the scalar magnetometer (left) and the vector magnetometer (VM) (right) with different configurations: tethers (T), fixed frame (F), and landing gear (L). Some configurations were flown additionally in reversed flight direction (indicated by the letter r in the labels). Dual sensor averages of the VM records are shown (letter a in the labels) with exemplarily results from the two individual sensors for the frame setup (labeled F1 and F2). The box-and-whisker plots show median values (green lines), the first and the third quartiles (horizontal blue lines), the range of the data (1.5 times the interquartile range, whiskers), and outliers (points outside the range).

in Table 4). Indeed, the fluctuation of the data compensated using the first set of compensation parameters (orange curve on Figure 5) is only slightly larger than when using the best set of parameters (green curve on Figure 5). On the other hand, we observe a significant difference in the averaged value of the compensated data depending on the set of parameters that was used (Figure 5, Table 4). The best set of compensation parameters yields an averaged value similar to the imposed absolute value of the field intensity with a precision of 0.1 nT. On the other hand, the first set of parameters yields a significant difference that seems to increase with time. This apparent drift in the averaged value is not due to diurnal variation which was accounted for in the estimation of the compensation parameters, but likely due to small changes in the properties of the magnetic sensors and platform.

4. Discussion

4.1. Comparison of the Different Configurations

Our goal was to design a fixed-frame magnetometer configuration to simplify flight maneuvers without sacrificing the accuracy of magnetic recordings. Indeed, the SM on tethers can be difficult to fly safely. Especially during take-offs and landings, the pilot must be careful to ensure that the tethers do not wrap around the legs or get caught in the propellers of the sUAS. The SM is usually stable when the aircraft flies along a straight line at high speed, but, even then, aircraft accelerations and rotations or crosswinds can cause swinging and twisting motions of the sensor system. This makes dense surveys difficult to fly (e.g., the system needs time to stabilize after each turn) and prohibits flights in complex terrain. On the other hand, our frame configuration offers improved in-flight stability. We were able to run flights fully autonomously including take-offs and landings. Moreover, the frame improved stability during take-offs and landings because of its wider base and more rigid construction relative to the landing gear. The frame configuration is suitable for pilots with little experience in flying magnetic sensors. While others have used fixed suspension methods for UAS-based magnetometry before (e.g., Gavazzi et al., 2019), the fixed suspension design that we propose can easily be used for commercial UAS magnetometer systems, both scalar and vector

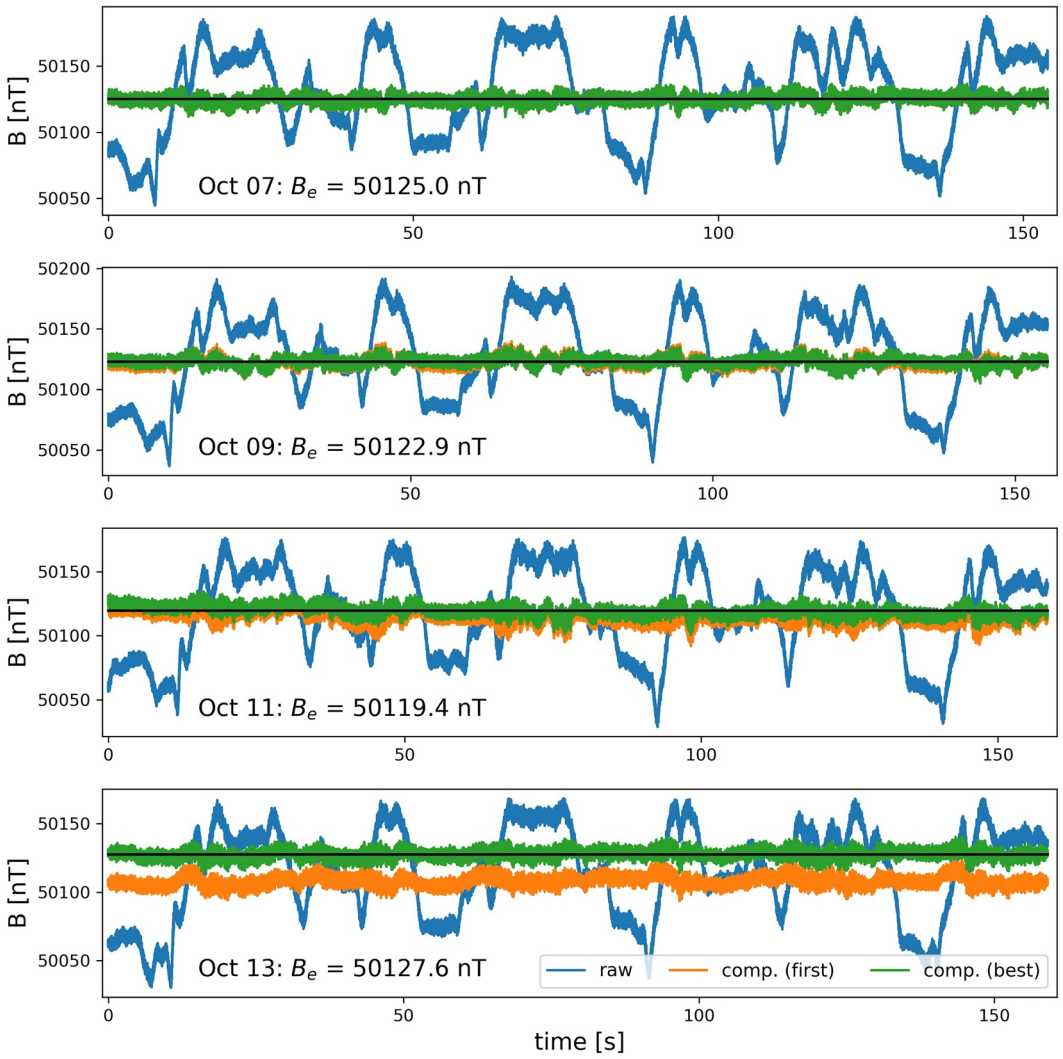

Figure 5. Comparison of the magnetic field intensity for the vector magnetometer (sensor 1) deduced from the raw recordings (blue) and compensated data (green and orange) collected for the same calibration pattern in Surprise Valley, CA on October 7, 9, 11 and 13. Recordings were compensated with the set of parameters deduced both from themselves (green, denoted best) and from the recordings of the first acquisition of the calibration pattern on October 7 (orange, noted first). The compensation is done assuming an arbitrary absolute intensity of the magnetic field of 50,125 nT at the time of the first acquisition of the calibration pattern (October 7), which is adjusted for the next acquisitions of the pattern based on the base-station data (value given by black line).

magnetometers. It leads to a compact system that is easy and safe to fly and it also has the potential to be employed for other sensors.

The accuracy of magnetic recordings from the frame construction are superior to recordings from the landing gear configuration, as can be seen in our analysis of standard deviations and cross-over differences. The poor accuracy of the landing gear configuration has several causes. First, sensors attached to the landing gear are closer to the aircraft. Even though only ~7 cm closer, the $1/r^3$ attenuation in point-source magnetic fields is significant. Second, the landing gear is attached only loosely to the sUAS used for our tests, which likely resulted in vibrations of the sensor. Additionally, since the data presented here were positioned using the GNSS signals from the magnetometer systems, GNSS signals for the landing-gear configuration could be adversely affected by the main body of the sUAS positioned directly above the GNSS sensors. However, the GNSS quality measures provided by the SM recordings (HDOP, fix quality, and number of satellites) suggested similar GNSS quality for all three configurations.

Table 4
Comparison of Standard Deviations (σ) and Averaged Values (μ) Deduced From the Compensated Recordings of the Calibration Patterns Whose Data are Plotted on Figure 5

Date	B [nT]	σ_{best} [nT]	σ_{first} [nT]	μ_{best} [nT]	μ_{first} [nT]	μ_{first} - μ_{best} [nT]
2020/10/07	50,125.0	3.6	3.6	50,125.0	50,125.0	0.0
2020/10/09	50,122.9	3.9	4.3	50,122.9	50,122.5	−0.4
2020/10/11	50,119.4	4.5	4.9	50,119.4	50,113.7	−5.6
2020/10/13	50,127.6	3.6	4.2	50,127.6	50,108.0	−19.6

Note. The table includes both results obtained using the best (denoted best) and first sets of compensation parameters (noted first). B is the absolute field intensity B assumed for the estimation of the best set of parameters, which was 50,125 nT at the time of the first acquisition of the calibration pattern (October 7) and was adjusted for following acquisitions of the pattern based on the base-station data.

The cross-over differences of the SM on tethers show an RMS error of 5.2 nT. This was computed without any compensation and shows the performance of the system. The magnetometer system includes two Cs-vapor magnetometers that have an intrinsic heading error of about 5 nT, according to the manufacturer (Geometrics, Inc., 2019). This agrees well with our results. Additional errors might arise from GNSS positioning errors (both in the horizontal and vertical direction) and in-flight swinging of the sensor system with respect to the sUAS. The surveys were flown at a constant elevation to minimize altitude differences at cross-over points. Since the test survey was flown with a relatively low speed of 7 m/s and relatively short line lengths of 100 m, sensor swing might have been larger than they would have been for a larger survey with long lines flown at high speeds. SM cross-over differences are lower with the frame configuration than with the tethered setup (RMS error of 3.3 nT and a much lower range as seen in Figure 4), indicating that we have corrected adequately for both the magnetic effects of the sUAS and some of the heading error of the magnetometer.

Although the uncompensated signals from sensor 1 are systematically characterized by larger standard deviations (σ_{raw}) and cross-over differences than sensor 2, we were able to reach a similar level in standard deviations (σ_{comp}) and cross-over differences of the compensated signals for both sensors. Since both sensors were located at the same distance from the sUAS, such difference in the uncompensated signal was likely due to a poorer manufacturer calibration of sensor 1. This suggests that the compensation method adequately corrects for inaccurate manufacturer calibration of the sensors. This result is consistent with results from Gavazzi et al. (2019) who observed that the standard deviation of the compensated signal from a VM used on different platforms is independent of the standard deviation of the uncompensated signal.

4.2. GNSS Positioning Data

The GNSS signals are critical not only for positioning but also to acquire accurate time information. The specifications from the sUAS GNSS are in general significantly better than from the magnetometer since the sUAS must rely on highly accurate positioning data for secure flights. To achieve this, the sUAS combines its GNSS data with signals from its IMU units. For reasons of redundancy, it does this for three combined GNSS/IMU units. After merging the GNSS data from the magnetometer systems and the sUAS, we observed significant differences in the positioning provided by these two receivers. The largest differences are as expected at the turning points of the surveys. However, differences over a straight line can be as large as several meters. Despite such differences, we observed that using the sUAS GNSS data instead of the magnetometer GNSS data did not improve the cross-over differences. Such absence of improvement might be due to the fact that the magnetic gradient in the survey area is small (see Figure 3) and a positioning error of a few meter introduces differences at cross-over points that are low compared to the observed RMS of cross-over differences. These are therefore likely dominated by other error sources.

4.3. Spectral Content of the Magnetic Recordings

The geomagnetic field recorded by the magnetometer systems is expected have relatively low frequencies. For instance, for a flight altitude of 30 m and a flight speed of 7 m/s, the largest frequency would be about 7/30 Hz ≈ 0.23 Hz assuming sources at ground level. However, the high sampling rates of our magnetometer systems, 1,000 Hz for the SM (Geometrics Inc., 2019) and 200 Hz for the VM (SENSYS, 2018), also capture high-frequency components that can reach amplitudes of several tens of nanoteslas as observed in Figure 2. Most of these high-frequency components can easily be removed by application of appropriate low-pass filters or when gridding the data. In the following, we discuss the power spectral densities (PSDs) of the SM and the VM recordings before and after compensation (Figure 6) to compare noise levels and identify signals that contribute to the measurements.

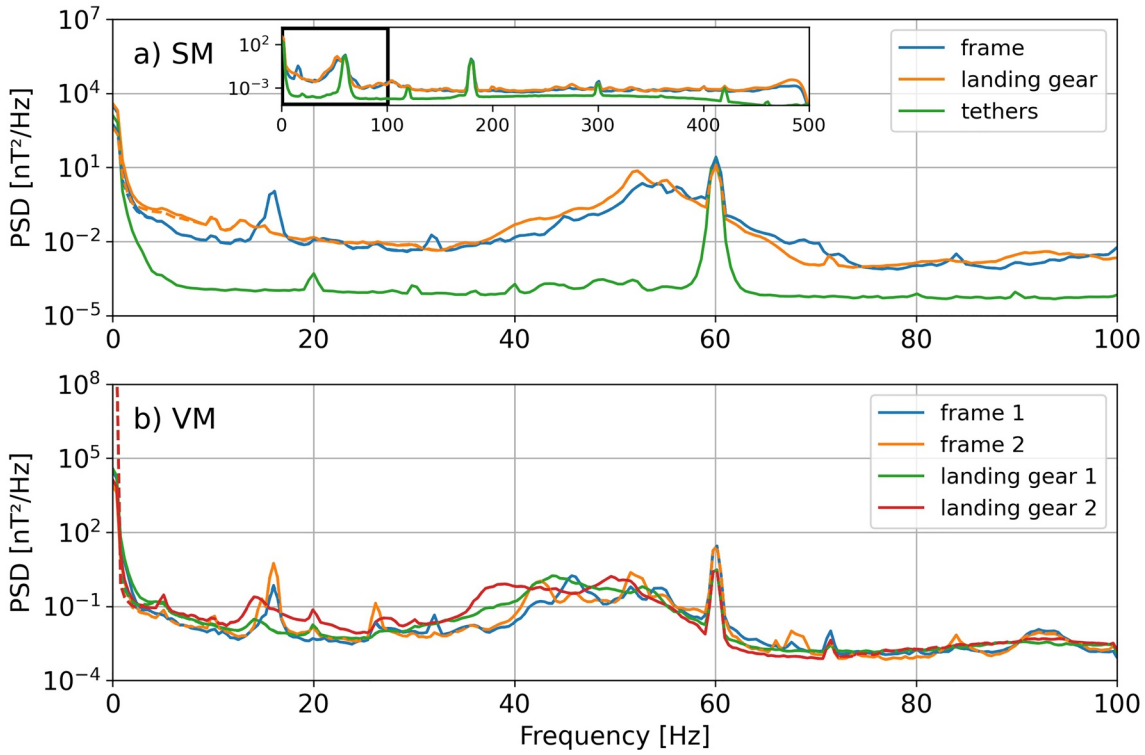

Figure 6. Power spectral density plots of the scalar magnetometer (SM) (a) and the vector magnetometer (VM) (b) recordings from the test survey data. The full frequency range of the SM is shown (inset plot in a) as well as only the first 100 Hz (black box in inset plot) for comparison with the VM data. For each sensor system and configuration, we show both the uncompensated (solid lines) and compensated signals (dashed lines).

The overall noise level of the tethered system is much lower than the noise level of the other configurations, because of the larger distance between the sensor and the sUAS. This sensor-sUAS distance is shortest for the landing gear setup, which is reflected in slightly larger amplitudes throughout the whole spectrum for the PSDs of the landing gear configurations compared to the frame configuration.

The signals of all configurations show a distinct peak at 60 Hz (Figure 6) caused by nearby power lines (the US power grid operates at 60 Hz) since the recordings used here were collected in an urban area. Several harmonics of that signal can also be observed in the SM recordings as peaks at 120 Hz, 180 Hz, 300 Hz, and 420 Hz (inset of Figure 6a).

Another peak at approximately 16 Hz, with a smaller peak at the 2nd harmonic at approximately 32 Hz, are observed in the recordings collected with the frame configuration. These peaks are observed with both sensor systems but are missing from the tethered and landing gear data leading us to conclude that this is a resonance frequency of the frame setup. This 16 Hz component observed with the frame setup could potentially cause a problem in the case of low elevation surveys flown at high speed over shallow sources of small dimensions, such as for the detection of unexploded ordnance or archeological studies. In this case, the signal of interest is of higher frequency than for large scale geologic studies and could therefore be in the same frequency band as the frame resonance. Future improvements to the frame setup should focus on dampening this resonance peak.

The broad peak in the range of 40–70 Hz with a maximum at approximately 50–53 Hz can be seen with both magnetometer systems regardless of the suspension except for the tethered flight. The SM shows a second broad peak slightly above 100 Hz. This range of frequencies is close to those of the propulsion system (motors and propellers) of the sUAS used in this study (DJI Technology Co., Ltd., 2016), which operate at 30–450 Hz, with the highest efficiency reached between 33 and 67 Hz according to the manufacturer. These contributions therefore likely originate from the rotation of the sUAS's motors, assuming the sUAS is mainly operating at the most efficient frequencies.

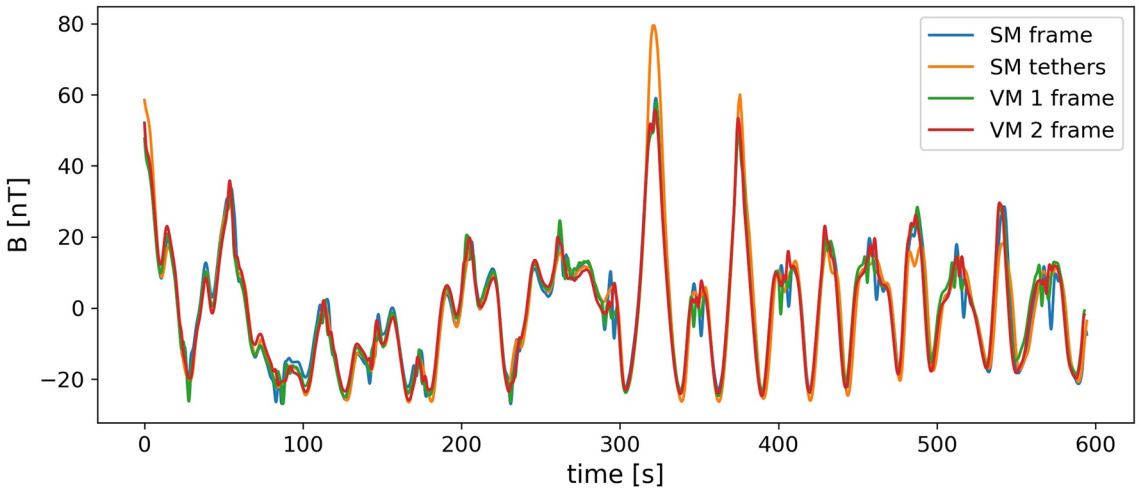

Figure 7. Low-pass filtered signals of the scalar magnetometer (frame and tethers) and the two vector magnetometer sensors (only frame) after compensation. The signals are shown after the mean of each survey was removed.

Both compensation methods used for the SM and VM correct for signals arising from changes in the attitude of the aircraft which are usually in the low frequency range. The compensation does not correct for signals that arise from the sUAS motors or other high-frequency components. Therefore, the spectra of the raw and the compensated signals look largely similar for high frequencies and show differences only in the 0–10 Hz range (Figure 6).

4.4. Absolute Adjustment of the Vector Magnetometer Relative Measurements

The VM calibration algorithm requires the value of the magnetic field intensity at the location of the calibration flight, which is usually unknown. Several estimations of this value can be used, including the International Geomagnetic Reference Field (IGRF) (Alken et al., 2021), the recording from an independent total field magnetometer (e.g., from a nearby base station also used for the diurnal correction), or simply recordings from the VM during the calibration flight (e.g., the average of the uncompensated field intensity). Since these estimations might all be different from the actual magnetic field intensity, the resulting intensity map usually includes a constant offset that is dependent on the magnetic field intensity used. This offset is irrelevant for obtaining an anomaly map (Munschy et al., 2007), however, it can be problematic when the newly acquired data are to be merged with older data from another system, or when the anomaly map is recorded through multiple flights spanned over a large time period (especially when multiple calibration flights were needed). Such problems can however be prevented with proper survey planning by including some overlap between the different surveys allowing to correct for offsets. Merging data from the VM acquired on distinct days with distinct calibration flights collected at the same location is also possible, however, it is important that the absolute intensity value used for the calibration of the VM compensation model is adjusted for diurnal variations.

When we compare compensation results using calibration flights from different days, we can see that the use of compensation parameters from six days ago introduce a general offset in the order of 20 nT (Figure 5 and Table 4). This is larger than the precision of our measurements showing that a new calibration is required every few days for the VM. We recommend flying the calibration pattern every day, as also advised by others (e.g., Gavazzi et al., 2020). Transport of the platform in the field could cause small accidental changes in the platform configuration that could modify the compensation parameters. Similar tests with the SM are planned in future investigations. If there are no temporal changes in the SM configuration or in the sUAS itself, there should be no need to repeat a compensation flight because the SM measures the absolute intensity of the magnetic field. Therefore, we expect the SM to require less frequent calibration flights.

To illustrate the good agreement of the compensated recordings, Figure 7 shows signals after their individual mean was removed to correct for the expected offset of the VM recordings (in this case ∼ 75 nT). The

signals have also been low-pass filtered using corner frequencies that resulted in minimum cross-over differences. Since the SM on tethers was flown 10 m below the other surveys, we upward-continued this signal to the flight altitude of the other surveys and resampled the data along the flight path. The larger differences between the tethered data with the other configurations data, which is significant mostly at a few maxima, are most likely an artifact from the upward-continuation procedure which involved interpolating the data on a regular grid (e.g., Blakely, 1996). The signals, after mean values are subtracted, are very similar with some spikes that were not corrected for by the compensation algorithms. These spikes occur mainly when the sUAS is at the end of a flight line and is turning towards the next line. However, this is not a problem since these segments are usually discarded from the data before creating an anomaly map.

5. Conclusion

We tested two magnetometer systems–scalar (SM) and vector (VM)–that are commercially available and designed for sUAS surveys by flying test surveys with various configurations for attaching each system to the aircraft. We present software that can be used to compensate for the magnetic fields arising from the sUAS. The software is adaptable to any fixed-frame design, platform, or sensor, and is therefore useful for future setups. We also developed a new suspension design using a fixed frame built from carbon fiber tubes and 3D-printed joints that offers more flight stability than the suspension methods recommended by the magnetometer manufacturers (tethers for the SM and attachment to the landing gear for the VM). Combined with algorithms to compensate for magnetic fields that originate from the sUAS, our frame setup also results in magnetic recordings of higher precision than the original suspension methods.

Suspending the SM on 2.8 m long tethers is the easiest configuration in terms of hardware requirements and data processing, and it does not require flying calibration maneuvers. It also provides data with far less noise in the high-frequency range. However, the sensor has an intrinsic heading error of ∼5 nT whose impact is further increased by swing motions of the system. Moreover, flying a tethered payload requires an experienced pilot, the design of flight missions that do not involve abrupt turns, and good flight conditions. The frame configuration is much more compact and therefore easier to fly. Flight missions can be carried out fully automatically (including take-offs and landings), in more windy conditions, and in complex terrain. Attaching the systems to the landing gear of the aircraft was relatively simple to deploy. However, we found that this configuration with our UAS platform results in significantly less accurate magnetic recordings.

The VM appears to provide more accurate results than the SM in any configuration. On the other hand, the SM directly records the absolute magnetic field intensity while the VM gives only a relative measurement of the intensity. The compensated magnetic field intensities of the VM will in most cases contain an offset which may be problematic when merging different datasets that do not overlap and were acquired at different time periods. This can often be prevented by proper survey planning that includes some overlap with previous surveys. One advantage of the SM over the VM is that the SM does not require manufacturer calibration while regular calibrations performed by the VM manufacturer are recommended. Such servicing of the VM is however not necessary if the survey planning includes calibration patterns that will allow to compensate miscalibration of the sensors. Finally, the VM offers vector information of the magnetic field that could also be used for recovering the three components of the magnetic field after further data processing (rotation to a fixed reference system and a three-component diurnal correction) and for magnetic gradiometry since it includes two sensors that are 1 m apart.

The frame configuration requires calibration flights in magnetically low-gradient areas, which might be sometimes difficult to find in the case of highly magnetic terrain, such as in volcanic provinces, that can show strong magnetic gradient even at the elevation of 120 m above ground level (e.g., Morrell et al., 2011). Calibration flights require additional time for planning and execution. However, the resulting magnetic recordings offer the lowest standard deviations and best cross-over differences, and therefore lowest heading errors, with both magnetometer systems in our tests. Regarding the VM, our result show that it is necessary to regularly update the calibration parameters with new calibration flights, one calibration flight every fieldwork day if possible. We plan to address the need for regular repeated compensation flights for the SM in a future study.

Overall, our study shows that aeromagnetic surveys using sUAS and commercially available magnetometer systems yield a precision of several nanotesla. With small hardware improvements and the use of compensation algorithms, we were able to significantly improve flight stability, which greatly simplifies flight maneuvers, while increasing the precision of the magnetic recordings over traditional methods.

Data Availability Statement

The data used in this study can be accessed online at https://doi.org/10.5066/P9KIU1OO (Kaub et al., 2021). The software MagComPy is open-source with a GNU AGPL-3.0 license and available at http://doi.org/10.5281/zenodo.4568692 (Kaub, 2021).

Acknowledgments
We thank Tait Earney, Branden Dean, Laurie Zielinski, Grant Rea-Downing, Nicholas Davatzes, Morgan Sawyer, and Pattawong Pansodtee for their great assistance during field experiments, Mircea Teodorescu for invaluable help in supporting this research, Naiema Jackson from Geometrics, Inc. for her support regarding the MagArrow system, and Richard Blakely and two anonymous reviewers for their constructive comments that significantly improved the manuscript. Grégory More contributed very helpful pieces of Python code. The magnetic survey used in this study were planned using the UgCS flight planning software (license through the UgCS educational program). This project was funded by the Geothermal Resources Investigation Project, under the Energy Program of the U.S. Geological Survey. During the course of this study, C. Bouligand was a visiting researcher at the U.S Geological Survey. ISTerre is part of Labex OSUG@2020 (ANR10 LABX56). Any use of trade, firm, or product names is for descriptive purposes and does not imply endorsement by the U.S. Government. Open access funding enabled and organized by ProjektDEAL.

References

Acuña, M. H. (2002). Space-based magnetometers. *Review of Scientific Instruments*, *73*(11), 3717–3736. https://doi.org/10.1063/1.1510570

Alken, P., Thébault, E., Beggan, C. D., Amit, H., Aubert, J., Baerenzung, J., et al. (2021). International geomagnetic reference field: The thirteenth generation. *Earth, Planets and Space*, *73*(1), 1–25. https://doi.org/10.1186/s40623-020-01281-4

Bertrand, L., Gavazzi, B., Mercier de Lépinay, J., Diraison, M., Géraud, Y., & Munschy, M. (2020). On the use of aeromagnetism for geological interpretation: 2. A case study on structural and lithological features in the Northern Vosges. *Journal of Geophysical Research: Solid Earth*, *125*(5), e2019JB017688. https://doi.org/10.1029/2019jb017688

Bickel, S. H. (1979). Small signal compensation of magnetic fields resulting from aircraft maneuvers. *IEEE Transactions on Aerospace and Electronic Systems*, *AES-15*(4), 518–525. https://doi.org/10.1109/TAES.1979.308736

Blakely, R. J. (1996). *Potential theory in gravity and magnetic applications* (p. 464). Cambridge university press. https://doi.org/10.1017/CBO9780511549816

Bouligand, C., Coutant, O., & Glen, J. M. (2016). Sub-surface structure of La Soufrière of Guadeloupe lava dome deduced from a ground-based magnetic survey. *Journal of Volcanology and Geothermal Research*, *321*, 171–181. https://doi.org/10.1016/j.jvolgeores.2016.04.037

Davis, K., Li, Y., & Nabighian, M. (2010). Automatic detection of UXO magnetic anomalies using extended Euler deconvolution. *Geophysics*, *75*(3), G13–G20. https://doi.org/10.1190/1.3375235

Dentith, M., & Mudge, S. T. (2014). *Geophysics for the mineral exploration geoscientist*. Cambridge University Press.

De Smet, T. S., Nikulin, A., Romanzo, N., Graber, N., Dietrich, C., & Puliaiev, A. (2020). Successful application of drone-based aeromagnetic surveys to locate legacy oil and gas wells in Cattaraugus county, New York. *Journal of Applied Geophysics*, *186*, 104250. https://doi.org/10.1016/j.jappgeo.2020.104250

DJI Technology Co, & Ltd (2016). *E2000 Pro user manual v1.4*. retrieved February 28, 2021, from https://dl.djicdn.com/downloads/e2000/20161220/E2000+Pro+User+Manual+V1.4.pdf

Douglas, D. H., & Peucker, T. K. (1973). Algorithms for the reduction of the number of points required to represent a digitized line or its caricature. *Cartographica: the international journal for geographic information and geovisualization*, *10*(2), 112–122. https://doi.org/10.3138/fm57-6770-u75u-7727

Fassbinder, J. W. E. (2017). *Magnetometry for Archaeology*. Encyclopedia of Geoarchaeology, 499–514. https://doi.org/10.1007/978-1-4020-4409-0_169

Finn, C. A., Deszcz-Pan, M., Ball, J. L., Bloss, B. J., & Minsley, B. J. (2018). Three-dimensional geophysical mapping of shallow water saturated altered rocks at Mount Baker, Washington: Implications for slope stability. *Journal of Volcanology and Geothermal Research*, *357*, 261–275. https://doi.org/10.1016/j.jvolgeores.2018.04.013

Gavazzi, B., Bertrand, L., Munschy, M., Mercier de Lépinay, J., Diraison, M., & Géraud, Y. (2020). On the use of aeromagnetism for geological interpretation: 1. Comparison of scalar and vector magnetometers for aeromagnetic surveys and an equivalent source interpolator for combining, gridding, and transforming fixed altitude and draping data sets. *Journal of Geophysical Research*, *125*, e2019JB018870. https://doi.org/10.1029/2019JB018870

Gavazzi, B., Le Maire, P., de Lépinay, J. M., Calou, P., & Munschy, M. (2019). Fluxgate three-component magnetometers for cost-effective ground, UAV and airborne magnetic surveys for industrial and academic geoscience applications and comparison with current industrial standards through case studies. *Geomechanics for Energy and the Environment*, *20*, 100117. https://doi.org/10.1016/j.gete.2019.03.002

Gavazzi, B., Le Maire, P., Munschy, M., & Dechamp, A. (2016). Fluxgate vector magnetometers: A multi-sensor device for ground, UAV and airborne magnetic surveys. *The Leading Edge*, *35*, 795–797. https://doi.org/10.1190/tle35090795.1

Geometrics (2019). *MagArrow UAS deployable magnetometer user guide V. 1 Rev.D*. retrieved April 10, 2021, from https://www.geometrics.com/wp-content/uploads/2019/10/MagArrow_LCS100S_User_Manual_V.1R.D.pdf

Hamoudi, M., Quesnel, Y., Dyment, J., & Lesur, V. (2011). Aeromagnetic and marine measurements. In Geomagnetic observations and models (pp. 57–103). Springer. https://doi.org/10.1007/978-90-481-9858-0_4

Hochstein, M. P., & Soengkono, S. (1997). Magnetic anomalies associated with high temperature reservoirs in the Taupo Volcanic Zone (New Zealand). *Geothermics*, *26*(1), 1–24. https://doi.org/10.1016/s0375-6505(96)00028-4

Kaub, L. (2021). *MagComPy: Initial release (Version v1.0.0)*. Zenodo. https://doi.org/10.5281/zenodo.4568692

Kaub, L., Glen, J. M. G., Bouligand, C., & Keller, G. (2021). *Aeromagnetic data collected to test new drone-based magnetometer configurations and magnetic compensation software; 2020 Santa Cruz, CA, and Surprise Valley, CA*. U.S. Geological Survey – ScienceBase Data Release. https://doi.org/10.5066/P9KIU1OO

Leliak, P. (1961). Identification and evaluation of magnetic-field sources of magnetic airborne detector equipped aircraft. *IRE Transactions on Aerospace and Navigational Electronics*, *ANE-8*(3), 95–105. https://doi.org/10.1109/tane3.1961.4201799

Le Maire, P., Bertrand, L., Munschy, M., Diraison, M., & Géraud, Y. (2020). Aerial magnetic mapping with an unmanned aerial vehicle and a fluxgate magnetometer: A new method for rapid mapping and upscaling from the field to regional scale. *Geophysical Prospecting*, *68*(7), 2307–2319. https://doi.org/10.1111/1365-2478.12991

Morrell, A. E., Locke, C. A., Cassidy, J., & Mauk, J. L. (2011). Geophysical characteristics of adularia-sericite epithermal gold-silver depositsin the Waihi-Waitekauri region, New Zealand. *Economic Geology*, *106*(6), 1031–1041. https://doi.org/10.2113/econgeo.106.6.1031

Munschy, M., Boulanger, D., Ulrich, P., & Bouiflane, M. (2007). Magnetic mapping for the detection and characterization of UXO: Use of multi-sensor fluxgate 3-axis magnetometers and methods of interpretation. *Journal of Applied Geophysics*, *61*(3–4), 168–183. https://doi.org/10.1016/j.jappgeo.2006.06.004

Nabighian, M. N., Grauch, V. J. S., Hansen, R. O., LaFehr, T. R., Li, Y., Peirce, J. W., et al. (2005). The historical development of the magnetic method in exploration. *Geophysics*, *70*, 33ND–61ND. https://doi.org/10.1190/1.2133784

Olsen, N., Clausen, L. T., Sabaka, T. J., Brauer, P., Merayo, J. M., Jørgensen, J. L., et al. (2003). Calibration of the Ørsted vector magnetometer. *Earth Planets and Space*, *55*(1), 11–18. https://doi.org/10.1186/bf03352458

Parvar, K., Braun, A., Layton-Matthews, D., & Burns, M. (2017). UAV magnetometry for chromite exploration in the Samail ophiolite sequence, Oman. *Journal of Unmanned Vehicle Systems*, *6*(1), 57–69.

Ramer, U. (1972). An iterative procedure for the polygonal approximation of plane curves. *Computer Graphics and Image Processing*, *1*(3), 244–256. https://doi.org/10.1016/s0146-664x(72)80017-0

Ripka, P. (1992). Review of fluxgate sensors. *Sensors and Actuators A: Physical*, *33*(3), 129–141. https://doi.org/10.1016/0924-4247(92)80159-Z

SENSYS Sensorik, & Systemtechnologie GmbH (2018). MagDrone R3 (from Rev. 3.03) Version 1.8.

Telford, W. M., Telford, W. M., Geldart, L. P., Sheriff, R. E., & Sheriff, R. E. (1990). *Applied geophysics*. Cambridge university press.

Tolles, W. E., & Lawson, J. D. (1950). Magnetic compensation of MAD equipped aircraft. *Airborne Instruments Lab. Inc., Mineola, NY, Rept, 201–1*.

Walter, C., Braun, A., & Fotopoulos, G. (2020). High-resolution unmanned aerial vehicle aeromagnetic surveys for mineral exploration targets. *Geophysical Prospecting*, *68*(1), 334–349. https://doi.org/10.1111/1365-2478.12914

Wessel, P. (2010). Tools for analyzing intersecting tracks: The x2sys package. *Computers & Geosciences*, *36*, 348–354. https://doi.org/10.1016/j.cageo.2009.05.009

Wessel, P., Luis, J. F., Uieda, L., Scharroo, R., Wobbe, F., Smith, W. H. F., & Tian, D. (2019). The generic mapping tools version 6. *Geochemistry, Geophysics, Geosystems*, *20*(11), 5556–5564. https://doi.org/10.1029/2019gc008515